applied sciences

MDPI

Article

Development of Fluorescence Imaging Technique to Detect Fresh-Cut Food Organic Residue on Processing Equipment Surface

Chansong Hwang [1], Changyeun Mo [2,*], Youngwook Seo [3], Jongguk Lim [3], Insuck Baek [1] and Moon S. Kim [1,*]

[1] Environmental Microbial and Food Safety Laboratory, Beltsville Agricultural Research Center, Agricultural Research Service, USDA, 10300 Baltimore Avenue, Beltsville, MD 20705, USA; chansong.hwang@usda.gov (C.H.); Insuck.Baek@usda.gov (I.B.)
[2] Department of Biosystems Engineering, College of Agricultural and Life Sciences, Kangwon National University, 1 Gangwon Daehakgil, Chuncheon-Si, Gangwon-Do 24341, Korea
[3] National Institute of Agricultural Sciences, Rural Development Administration, 310 Nonsaengmyeong-ro, Wansan-gu, Jeonju-si, Jeollabuk-do 54875, Korea; yws25@korea.kr (Y.S.); limjg@korea.kr (J.L.)
* Correspondence: cymoh100@kangwon.ac.kr (C.M.); Moon.Kim@usda.gov (M.S.K.); Tel.: +82-33-250-6494 (C.M.); +1-301-504-8462 (M.S.K.); Fax: +82-33-259-5561 (C.M.); +1-301-504-9466 (M.S.K.)

Abstract: With increasing public demand for ready-to-eat fresh-cut food products, proper sanitation of food-processing equipment surfaces is essential to mitigate potential contamination of these products to ensure safe consumption. This study presents a sanitation monitoring technique using hyperspectral fluorescence images to detect fruit residues on food-processing equipment surfaces. An algorithm to detect residues on the surfaces of 2B-finished and #4-finished stainless-steel, both commonly used in food processing equipment, was developed. Honeydew, orange, apple, and watermelon were selected as representatives since they are mainly used as fresh-cut fruits. Hyperspectral fluorescence images were obtained for stainless steel sheets to which droplets of selected fruit juices at six concentrations were applied and allowed to dry. The most significant wavelengths for detecting juice at each concentration were selected through ANOVA analysis. Algorithms using a single waveband and using a ratio of two wavebands were developed for each sample and for all the samples combined. Results showed that detection accuracies were better for the samples with higher concentrations. The integrated algorithm had a detection accuracy of 100% and above 95%, respectively, for the original juice up to the 1:20 diluted samples and for the more dilute 1:50 to 1:100 samples, respectively. The results of this study establish that using hyperspectral imaging, even a small residual quantity that may exist on the surface of food processing equipment can be detected and that sanitation monitoring and management is possible.

Keywords: fresh-cut food; hyperspectral fluorescence; stainless steel; organic residue; detection

Citation: Hwang, C.; Mo, C.; Seo, Y.; Lim, J.; Baek, I.; Kim, M.S. Development of Fluorescence Imaging Technique to Detect Fresh-Cut Food Organic Residue on Processing Equipment Surface. *Appl. Sci.* **2021**, *11*, 458. https://doi.org/10.3390/app11010458

Received: 12 November 2020
Accepted: 30 December 2020
Published: 5 January 2021

1. Introduction

Increasing consumption of prepackaged, ready-to-eat fresh-cut foods by people living in busy urban areas has been accompanied by a growing need to ensure food safety and stability, in part due to the occurrence of multiple outbreaks of foodborne illnesses [1]. Although any field-harvested produce can include contaminants such as bacteria, worms, or feces, [2–4], microbial growth can occur more easily after fresh-cut processing and thus, fresh-cut products are often more perishable and more vulnerable to pathogens [5]. Incomplete cleaning and sanitation of equipment used to handle these products, such as pumps, tanks, and containers, can lead to cross-contamination of food products. Contamination on the surfaces of food processing equipment is a potential cause of pathogen transmission to finished products of food-processing procedures [6,7]. Food residue remaining on equipment surfaces can shield bacteria from sterilization and drying stress [8]. To reduce

the risk of contamination of agricultural products during such processing, it is necessary to develop better sanitation monitoring systems [9].

Sanitation monitoring of processing surfaces in food processing facilities is primarily a manual operation (e.g., visual inspection) conducted by inspectors according to established guidelines [10]. The conventional sanitary inspection method, namely, microbial contamination inspection, involves identifying a potentially contaminated location, collecting samples from the surface of this location, culturing the microorganism(s) for a period of one to three days, and as counting single organisms is very difficult. This microbial culturing process is tedious, requiring laboratory operations. Nucleic-acid-based methods are more sensitive than traditional culture-based methods because they enable detection of the DNA or RNA sequences of specific pathogens; however, they require skilled experts and expensive equipment and are also tedious [11,12]. These methods can be used to measure different contamination levels in one area corresponding to the sampling location, and the number of samples obtained via these methods is limited by the analysis equipment and the analysis period. Therefore, monitoring techniques, which can enable rapid measurement of the contamination levels without limiting the number of samples and the sampling locations, are required. A system that can rapidly and accurately detect the presence of vectors for pathogen growth on the surfaces of food processing equipment is especially needed to enhance food safety [13].

Various imaging and spectroscopic technologies have been researched for the rapid detection of contamination in foods and food processing facilities [14,15]. Particularly, hyperspectral imaging technology, which combines imaging and spectroscopy techniques, facilitates nondestructive measurement, involving the acquisition of spatial and spectral information simultaneously for each pixel in a sample image [16]. It can also facilitate mapping of the differences in the physical, chemical, and biological properties of a target object into a spatial distribution, and monitoring of the entire surface of the target object in real time. This technology has been studied in recent years for application in fields such as food safety inspection, quality identification of agricultural products, and biological contaminant detection [17], alongside, analysis techniques such as spectral unmixing and multivariate analysis-based band selection and classification have also been investigated for obtaining meaningful information from vast hyperspectral data. In the food industry, non-destructive measurements are applied to evaluate food quality and safety by collecting and analyzing the characteristics of agricultural products, such as the physical attributes and chemical content [18–24]. Other hyperspectral imaging applications have addressed environmental, defense, and biomedical areas, based on deep learning technology [25].

Hyperspectral fluorescence imaging is a sensitive optical technique that uses selected light excitation of a sample to induce light emissions from the sample at wavelengths different from the excitation light of 365 nm [6,22,26]. In studies targeting detection of bacterial biofilm, feces, organic residues, and insects in agricultural produce for food safety, non-destructive and non-contact fluorescence imaging using fluorescence regions from 480 to 560 nm and from 670 to 690 nm has been demonstrated to be an effective technique for rapid detection of contaminants [6,16,26–31].

The aim of this study is to investigate a hyperspectral fluorescence imaging technique for rapid detection of fruit residues on the surfaces of stainless steel food processing equipment, which can potentially harbor bacteria if inadequately cleaned. In particular, this study focuses on fresh fruit residues on 2B-finished and #4-finished stainless steel, which are commonly used in food processing equipment [32]. Fluorescence imaging characteristics are investigated for apple, orange, honeydew melon, and watermelon residues on 2B- and #4-finished stainless steel, and a residue-detection algorithm is developed using optimal waveband selected for each type of fruit residue.

2. Materials and Methods

2.1. Sample Preparation

Fresh-cut honeydew melon, orange, apple, and watermelon were purchased from local markets. Each fruit was blended and pressed to prepare juice to apply as residue to 2B-finished and #4-finished stainless steel sheets (SSS). For each of the four fruits, six juice concentrations were prepared: first, a stock solution from the initial pressing, followed by five diluted solutions prepared at ratios of 1:5, 1:10, 1:20, 1:50, and 1:100 with distilled water. Fifteen 10-uL droplets of each concentration were applied on the surface of each of the two types of SSS and allowed to dry at ambient room temperature (26 °C for 24 h. For each fruit, 90 droplets (6 sets with 15 droplets) for each of the 6 concentrations were applied onto each of the two types of SSS, for a total of 540 droplets were used for hyperspectral fluorescence imaging.

2.2. System and Data Acquisition

The tabletop hyperspectral fluorescence line-scan imaging system used in this study is shown in Figure 1. The hyperspectral fluorescence imaging system comprises a hyperspectral imaging device, transfer table, and ultraviolet-A (UV-A) light source. To identify food components such as chlorophyll a, UV-A (365 nm) excitation light, whose fluorescence emission range is in the blue-to-near-infrared region (up to 730 nm), was used [32]. The imaging device comprises a 14-bit electron-multiplying charge-coupled-device (EMCCD) camera (MegaLuca R EMCCD camera, Andor Technology PLC, Belfast, Northern Ireland), spectrograph (Hyperspec VS imaging spectrograph, Headwall Photonics, Fitchburg, MA, USA) with a 60-µm slit and a C-mount lens (Schneider-Xenoplan 1.4/23 C-mount lens, Schneider Optics, Hauppauge, NY, USA). The transfer table includes a step motor (Velmex, Bloomfield, NY, USA) and linear motion guide. The UV-A light source is composed of two pairs of four 10-W light-emitting diodes (LEDs; LedEngin, San Jose, CA, USA) that emit excitation light at 365-nm [26].

Hyperspectral line-scan images of the juice residues on SSS were obtained by moving the samples by 740 steps at 0.5 nm per step for an exposure time of 0.2 s in a darkened room. Each line-scan contained 502 × 501 spatial pixels obtained by pairwise binning (averaging) of the 1004 × 1002 available pixels in the spatial dimension, and 70 wavebands spanning 450–730 nm in the spectral dimension that were obtained by binning at approximately 4 nm intervals. Since the wavelength region after 730 nm is a region that is repeated as the effect of second order, this region was removed by a filter (Kodak Wratten Gelatin Filter, No. 8, Kodak, Rochester, NY, USA). Through this acquisition process, hyperspectral image cubes composed of 502 × 501 × 70 (spatial × spatial × spectral) were collected using the in-house developed software [10,26].

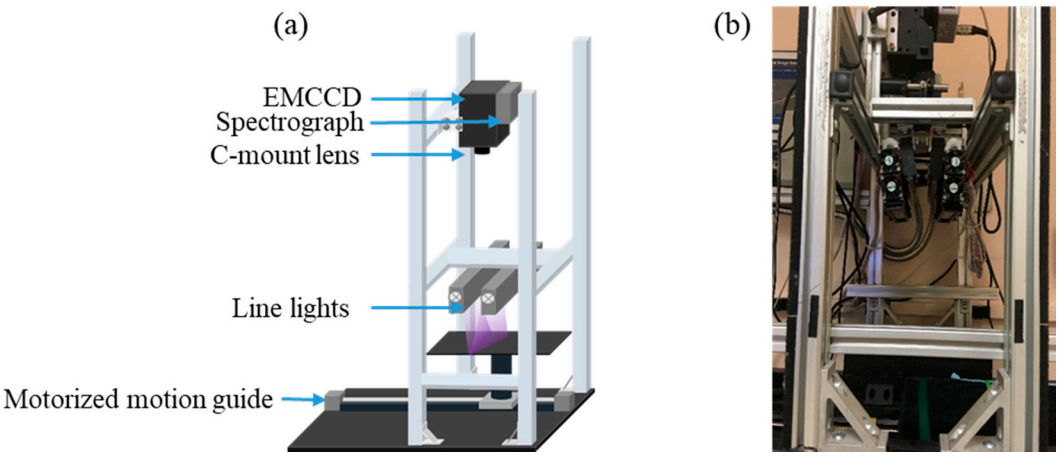

Figure 1. (**a**) Illustration and (**b**) photo of the hyperspectral imaging system.

2.3. Data Analysis

The collected hyperspectral fluorescence images were calibrated using a dark reference image, and a flat-field image shows that fluorescence was exhibited uniformly [33].

$$I(i) = (I\_s\ (i) - D(i))/(I\_r(i) - D(i)), \quad (1)$$

where I is the corrected relative hyperspectral fluorescence image, Is is the sample hyperspectral fluorescence image, Ir is the hyperspectral fluorescence image of the fluorescent reference plate, and D is the hyperspectral image of the dark reference plate, all at the i-th wavelength.

The fluorescence spectra of the pixels composed of fruit juice residues and the SS surfaces were extracted from the corrected fluorescence hyperspectral images and used to calculate the average fluorescence spectrum. The spectra were extracted from the region of interest (ROI) of the juice residue spots on the SSS in the corrected fluorescence image. The ROI comprises the region from the center to the boundary of the residue, and 15–25 pixels per droplet were selected in this region.

As shown in Figure 2, algorithms were developed for detecting residues using a single waveband (SW) and a ratio of two wavebands. Data analysis was performed as follows. The SW algorithms were developed using the fluorescence intensity of one waveband, and the two waveband ratio (TWR) algorithms were developed using the ratio of the fluorescence intensity of two wavebands. The optimal wavebands for identifying the residues of each fruit and the SSS were determined via one-way analysis of variance (ANOVA) of the extracted spectra. The spectra extracted from the ROI were divided into two groups, namely, clean surface and residue, and labelled as 0 and 1, respectively. One-way ANOVA was performed on all 70 wavebands in the 450–730 nm region to differentiate between the two groups. The F-value obtained via the ANOVA analysis for an SW and the ratio of two wavebands was used to select the optimal wavebands [22,30]. A larger F-value represents a more statistically significant mean separation between the two groups.

Optimal bands were selected using the calibration data set for the six dilution concentrations of each fruit residue on two types of SS surfaces. The SW algorithms and TWR algorithms were developed using the selected optimal band, and these models were verified using a validation set. The data sets for the calibration and validation were randomly divided into 80% and 20% of the total data, respectively.

The calibration algorithm determines the threshold value that has the highest residue detection accuracy in the calibration data set, and the detection accuracy of the validation model is determined by applying this threshold value to the validation data set. In addition, a global detection algorithm was developed that can be applied to the residues of all four types of fruits.

The global residue detection image algorithm was developed by applying the developed global detection algorithm to the hyperspectral fluorescence images. A two waveband ratio image (TWRI) algorithm was developed using the ratio image of two wavebands selected in the TWR algorithm according to Equation (2).

$$\mathrm{RIa/b} = \frac{Ia}{Ib}, \quad (2)$$

where I_a and I_b denote the corrected images at wavebands a and b, respectively.

Imaging algorithms were developed to use an SW and a TWR to detect juice residue on the SS surfaces. A binary image composed of black of a clean surface with '0' and white of the residue with '1' was generated by applying the threshold value to the image with the selected waveband, and the regions in white were identified as residues. The detection accuracy of the residues refers to the number of positives wherein the residues are correctly identified. Image processing, data extraction, and analysis were performed using MATLAB (Version R2016b, MathWorks, Inc., Natick, MA, USA, 2016).

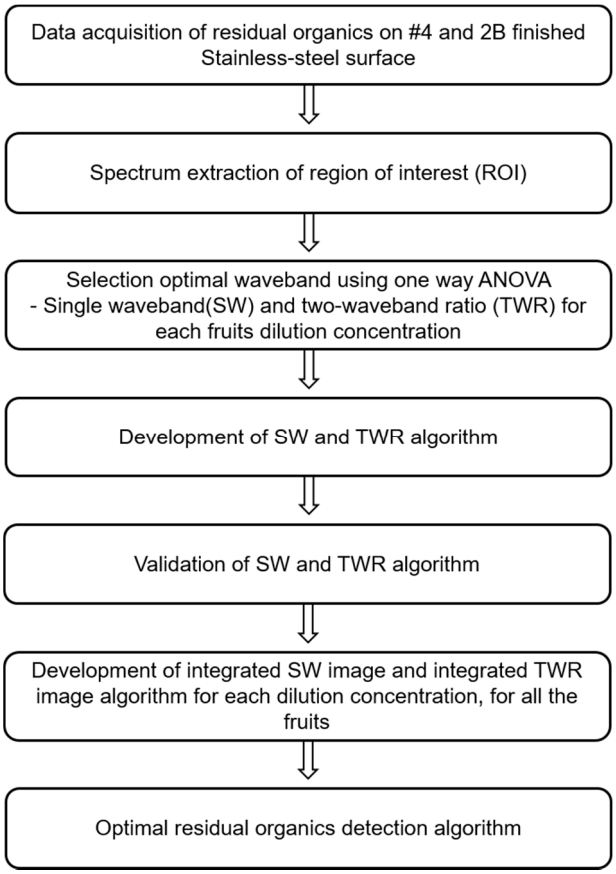

Figure 2. Flowchart for the development of the optimal residual-organic detection algorithm.

3. Results and Discussion

3.1. Fluorescence Characteristics of Stainless Steel and Fruits Samples

Generally, 2B-finished stainless-steel has a smooth surface and slight reflection similar to a mirror, while #4-finished stainless steel has a fine-polishing grit line with uniform appearance and directionality on its brushed surface [34].

Figure 3 shows the fluorescence spectra of the two types of stainless steel. The 2B spectrum has a characteristic broad fluorescence peak in the 600–740 nm range, while the #4 spectrum is relatively flat at all wavelengths across the 450–730 nm range.

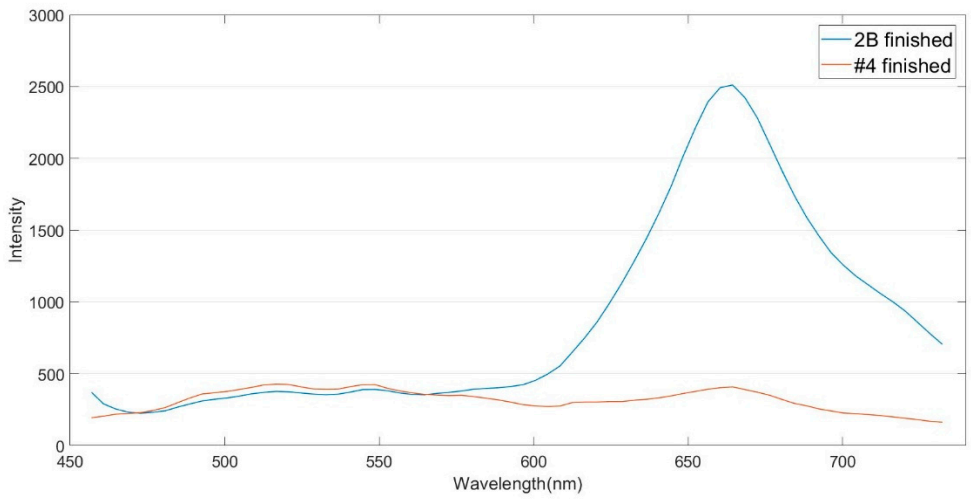

Figure 3. Average spectra of the stainless-steel surfaces.

Figure 4 shows, for each fruit, the average spectra for each concentration of juice residue on the surfaces of 2B-finished SSS. All the samples show a broad fluorescence peak in the 600–740 nm region similar to that of the 2B-finished stainless steel spectrum in Figure 3.

The honeydew residue spectra show a tendency for fluorescence peak intensities in the 450–600 nm range to decrease with increasing dilution (decreasing juice concentration); the most diluted samples (1:100) show nearly the same fluorescence properties as 2B stainless steel in this region. In the 600–730 nm range, the fluorescence peaks of stainless steel are the highest, and the 1:5, 1:20, 1:50, and 1:100 dilutions also exhibit fluorescence properties similar to those of the 2B stainless steel.

Similarly, the orange residue spectra show a decrease in fluorescence peak intensity with the increasing dilutions for the 450–600 nm range. Again, in the 600–730 nm region, the peak values of 2B stainless steel are the highest, and there are almost no differences in the fluorescence peaks for all the dilution concentrations.

The apple residue spectra also show a decrease in the fluorescence peak intensity with the increasing dilutions for the 450–600 nm range; the values for the 1:5 and 1:10 samples increase, whereas the remaining samples show fluorescence properties similar to those of stainless steel. In the 600–730 nm region, the fluorescence peak of stainless steel is the highest, and there are differences between the fluorescence peaks exhibited by the original juice and the 1:5 dilution concentration. However, there are almost no differences among the fluorescence peaks at the other dilution concentrations.

The watermelon residue spectra also show a decrease in fluorescence peak intensities in the 450–600 nm range with increasing dilution; the values for the 1:5, 1:10, and 1:20 samples increase, whereas the remaining samples exhibit fluorescence properties similar to those of stainless-steel. In the 600–730 nm range, the peak value of stainless steel is the highest, and there are almost no differences among the fluorescence peaks at all the dilution concentrations.

On the 2B finished surface, all the fruits used in the experiment show significant differences in the spectra for the different concentrations in the 450–600 nm range. In the 600–730 nm range, the peak value of stainless-steel is the highest for all four fruits, and it is difficult to distinguish based on the dilution concentration. The 450–600 nm and 600–730 nm ranges are known to be related to carotenoids and chlorophyll characteristics, respectively [35–37].

Figure 5 shows, for each fruit, the average spectra for each concentration of juice residue on the surfaces of #4-finished SSS. For all the fruits, the original juice exhibits the highest fluorescence intensities and the #4 surface has much less influence on the juice residue spectra in Figure 5 compared to the influence of the 2B surface in the juice residue spectra in Figure 4. In the 450–600 nm range, all the samples have fluorescence properties similar to those of #4-finished SSS. In the 650–690 nm range, the original juice, and the 1:5 and 1:10 dilution samples exhibit intensities much higher than the #4 SSS does, whereas the spectra of the remaining dilution samples are more similar in intensity and in their trend with concentration.

In the 450–600 nm range, the spectra of the honeydew residue on #4 SSS show a decrease in fluorescence peak intensities with each sequential dilution of the original juice. Although the spectra of the original juice and the first three dilutions are very clearly distinguishable, but those of the two most dilute samples (1:50 and 1:100) are not. In the 600–730 nm range, the original juice and the 1:5 dilution can be distinguished but the four remaining dilutions cannot.

The spectra of the orange residue on #4 SSS show decreasing fluorescence intensity with increasing dilution in the 450–600 nm range, similar to that of the honeydew residue spectra. In the 600–730 nm range, clearly distinguishable fluorescence peaks are observed for the original juice and for the 1:50 and 1:100 dilution samples.

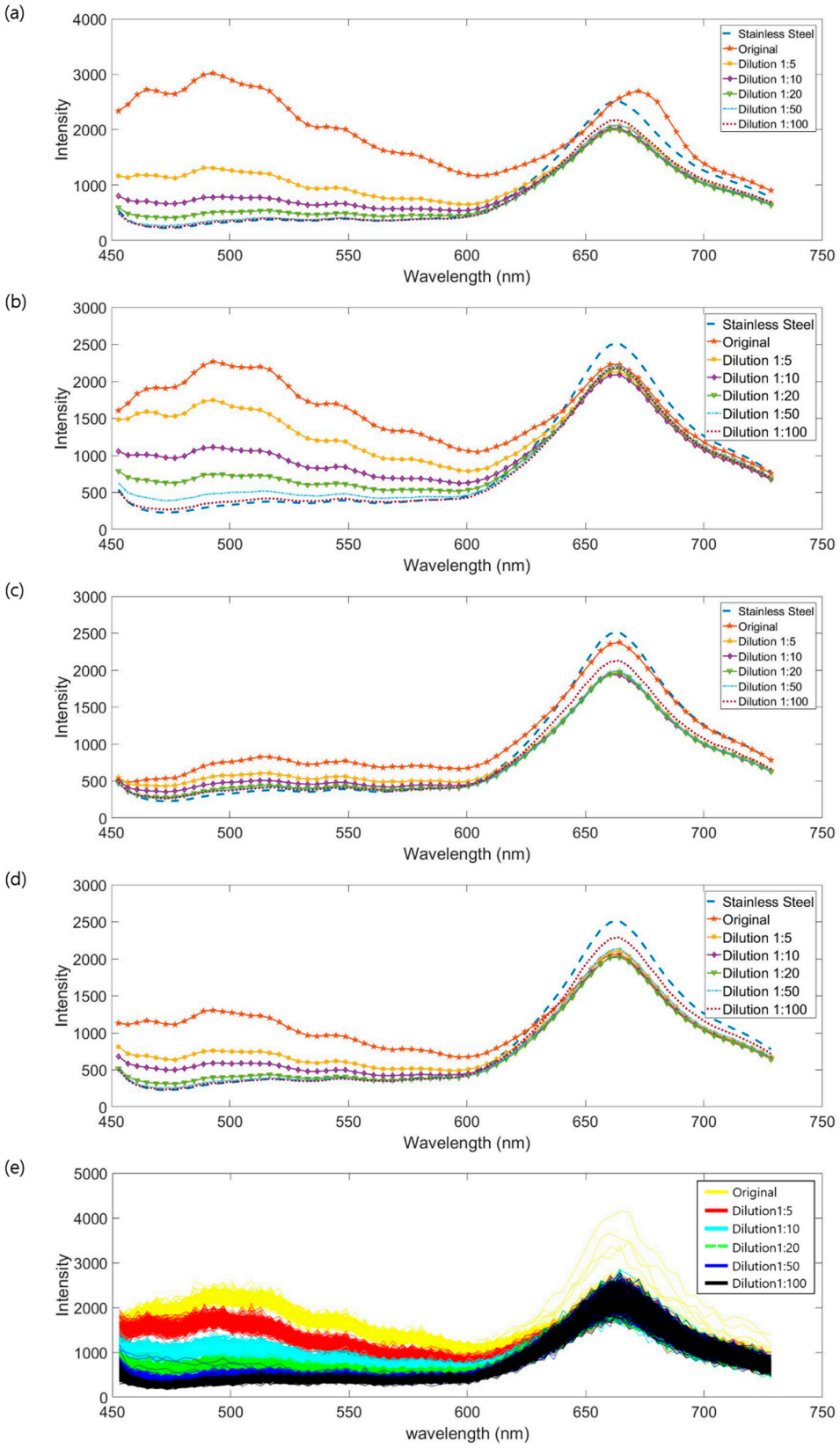

Figure 4. Average spectra of fruit juice residues on the 2B-finished stainless steel: (**a**) honeydew; (**b**) orange; (**c**) apple; (**d**) watermelon; and (**e**) raw pixel spectra extracted from one droplet of orange juice residues on the 2B-finished stainless steel.

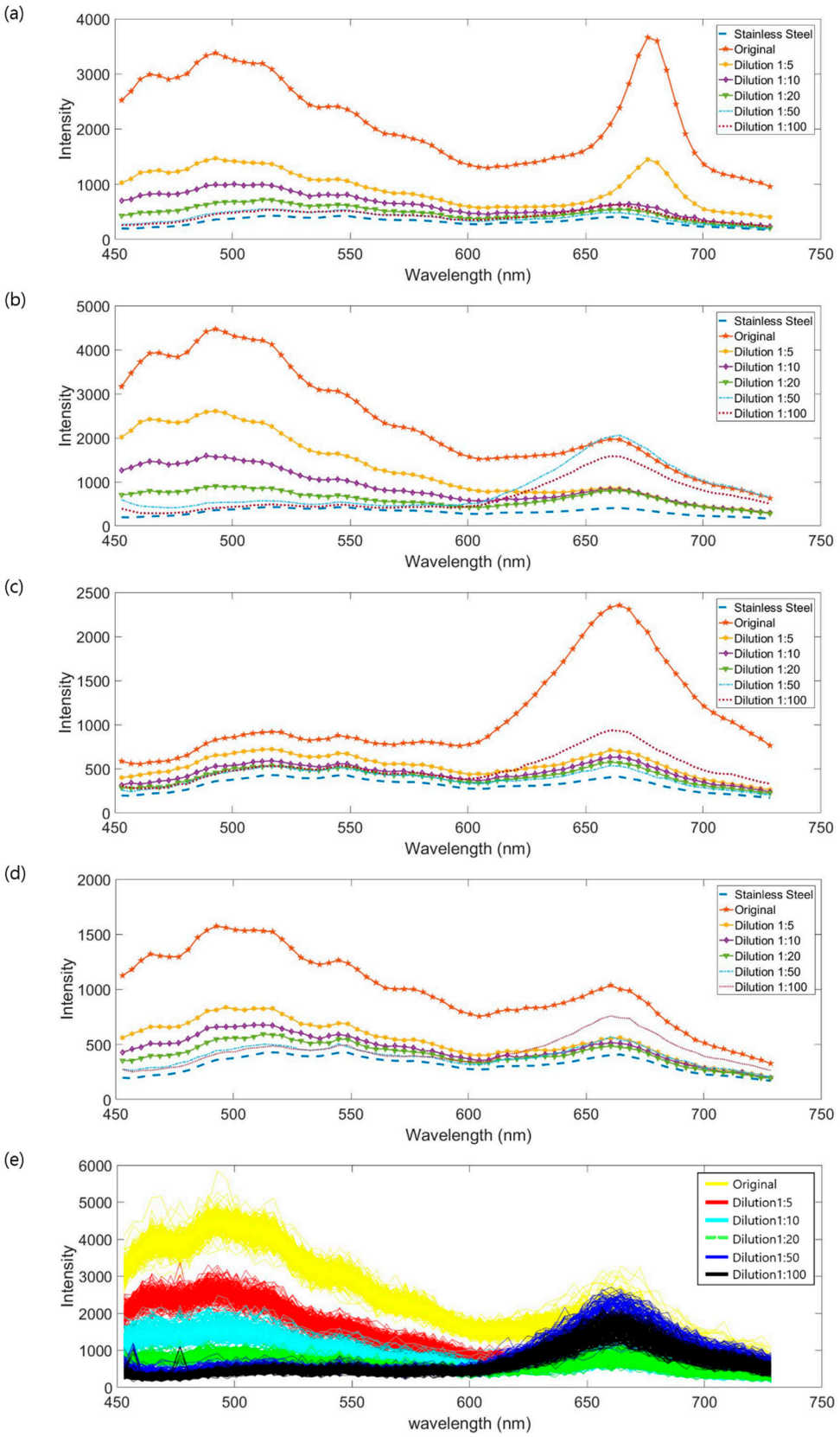

Figure 5. Average spectra of fruit juice residues on the #4-finished stainless steel: (**a**) honeydew; (**b**) orange; (**c**) apple; (**d**) watermelon; and (**e**) raw pixel spectra extracted from one droplet of orange juice residues on the #4-finished stainless steel.

The spectra of apple residue on #4 SSS show a similar pattern of decreasing fluorescence intensity with increasing dilution in the 450–600 nm range, with the original juice and the 1:5 and 1:10 dilutions being the most distinct. The remaining samples have spectral properties similar to those of stainless steel. In the 600–730 nm range, the high intensity fluorescence peak decreases as the dilution increases for the six juice concentrations.

The spectra of watermelon residue on #4 SSS show a similar pattern to those of honeydew and orange in the 450–600 nm range, with decreasing fluorescence peak intensities with each sequential dilution of the original juice and distinguishable spectra for the original juice and the first three dilutions, but non-distinguishable spectra for the two most dilute samples (1:50 and 1:100). In the 600–730 nm range, the original juice and the 1:10 dilution clearly show a high intensity spectral peak but the spectra of the four remaining dilutions are not distinguishable.

All the fruits show features in common on the 2B-finished as well as #4-finished surfaces. The broad peaks in the 450–600 nm range are presumed to be due to the complex composition of components that affect sugar content, such as glucose, or the components of flavonoids and carotenoids. The peak between 600–730 nm may to be due to chlorophyll [6,35,38–43].

3.2. Optimal Waveband Selection Using ANOVA Analysis Results

ANOVA analysis was performed according to the two types of SS surfaces and fruit juice dilution levels in order to select the optimal wavebands for detecting residue contamination. Figures S1–S6 show the F-value of the one-way ANOVA for classifying two types of SS surfaces and four types of fruit residues using the SW and the TWR. The optimal wavebands and classification results for each algorithm in terms of residue detection using the pixel spectra are shown in Tables 1–4.

Table 1. Optimal wavebands and discrimination algorithm results using the single-waveband method for 2B-finished stainless steel sheets (SSS).

	Dilution	2B-Finished SSS						
		Waveband [nm]	F-Value	Calibration			Validation	
				No. of Spectra	TH	Accuracy [%]	No. of Spectra	Accuracy [%]
Honeydew	original	492	106,900	1548	1983	92.92	386	92.94
	1:5	472	43,074	1570	827	91.56	392	91.45
	1:10	488	11,786	1604	545	86.86	400	86.99
	1:20	484	3666	1617	362	86.33	404	83.99
	1:50	648	1437	1630	1742	75.78	407	70.46
	1:100	644	353	1536	1563	69.08	383	67.25
Orange	original	488	112,939	1290	1891	92.30	322	92.55
	1:5	468	78,675	1620	1242	90.88	405	91.04
	1:10	468	32,946	1590	800	87.52	397	87.68
	1:20	484	16,047	1592	495	85.40	398	85.67
	1:50	480	3090	1444	332	80.08	360	80.01
	1:100	644	464	1476	1585	72.55	368	72.67
Apple	original	488	15,440	1504	481	93.38	375	93.37
	1:5	488	6618	1731	415	86.16	432	85.29
	1:10	488	2913	1533	382	85.16	383	83.86
	1:20	648	1579	1519	1707	82.79	379	81.30
	1:50	644	745	1220	1556	80.06	305	75.54
	1:100	648	536	1131	1825	73.65	282	73.00
Watermelon	original	488	24,763	1687	861	85.35	421	85.73
	1:5	468	14,236	1592	487	82.74	398	82.71
	1:10	484	4000	1535	382	82.94	383	82.78
	1:20	472	1324	1448	260	82.55	362	78.10
	1:50	644	796	1420	1555	75.48	355	70.55
	1:100	644	149	1408	1642	67.53	351	60.02

Note: TH = Threshold value.

Table 2. Optimal wavebands and discrimination algorithm results using the single-waveband method for #4-finished SSS.

	Dilution	#4-Finished SSS						
		Waveband [nm]	F-Value	Calibration			Validation	
				No. of Spectra	TH	Accuracy[%]	No. of Spectra	Accuracy [%]
Honeydew	original	508	59,703	1702	1857	92.55	425	92.54
	1:5	488	11,384	1636	688	92.25	408	92.19
	1:10	468	6652	1531	429	90.68	382	91.91
	1:20	484	2110	2052	459	90.50	512	89.88
	1:50	484	314	1460	388	69.73	365	63.42
	1:100	660	1318	1465	483	68.70	366	65.64
Orange	original	492	193,159	1844	620	98.23	461	98.10
	1:5	464	66,281	1771	1422	91.15	442	91.37
	1:10	464	18,748	1592	1003	91.47	397	91.66
	1:20	464	10,785	1987	454	92.98	496	92.74
	1:50	668	15,079	1527	577	92.72	381	92.85
	1:100	660	17,562	1775	994	89.81	443	89.75
Apple	original	584	9260	1672	677	85.81	418	85.17
	1:5	480	3512	1861	344	82.48	465	79.47
	1:10	468	1509	1763	338	83.55	440	72.34
	1:20	652	1073	2076	433	80.63	518	77.48
	1:50	656	359	1570	437	71.83	392	70.04
	1:100	672	2521	1431	487	70.02	357	69.06
Watermelon	original	460	26,669	2246	791	89.04	561	89.22
	1:5	464	5731	1555	434	87.71	388	86.91
	1:10	464	2845	1551	340	88.54	387	86.03
	1:20	460	1401	1984	290	83.36	495	77.82
	1:50	652	928	1576	409	77.91	394	69.30
	1:100	672	2414	1471	486	71.74	367	70.76

Note: TH = Threshold value.

Table 3. Optimal two wavebands and discrimination algorithm results using the two-waveband method for 2B-finished SSS.

	Dilution	2B-Finished SSS							
		Ratio Waveband [nm]		F-Value	Calibration			Validation	
					No. of Spectra	TH	Accuracy [%]	No. of Spectra	Accuracy [%]
Honeydew	original	460	656	2396	1548	0.98	91.79	386	92.44
	1:5	460	660	2089	1570	0.40	90.56	392	91.63
	1:10	460	676	1306	1604	0.34	87.51	400	88.67
	1:20	472	652	809	1617	0.18	85.40	404	84.36
	1:50	476	656	344	1630	0.15	79.19	407	78.23
	1:100	472	652	95	1536	0.14	74.84	383	73.43
Orange	original	456	660	2614	1290	0.43	92.30	322	92.36
	1:5	460	652	2400	1620	0.63	90.96	405	91.84
	1:10	472	640	2011	1590	0.44	90.06	397	90.36
	1:20	460	660	1358	1592	0.28	88.48	398	88.62
	1:50	468	652	767	1444	0.17	84.90	360	85.79
	1:100	472	644	270	1476	0.17	74.37	368	72.02
Apple	original	472	644	2058	1504	0.21	93.12	375	92.90
	1:5	464	640	505	1731	0.70	89.07	432	89.53
	1:10	472	644	1213	1533	0.20	88.22	383	87.53
	1:20	484	656	1084	1519	0.16	87.63	379	83.90
	1:50	488	648	958	1220	0.19	83.95	305	76.09
	1:100	472	652	172	1131	0.11	77.02	282	72.91
Watermelon	original	460	656	1237	1687	0.56	87.31	421	93.31
	1:5	464	640	1178	1592	0.41	87.15	398	90.67
	1:10	472	632	1131	1535	0.32	87.31	383	87.45
	1:20	464	644	654	1448	0.20	84.39	362	82.06
	1:50	468	648	161	1420	0.18	77.57	355	80.33
	1:100	472	580	105	1408	0.70	64.71	351	63.36

Note: TH = Threshold value.

Table 4. Optimal two wavebands and discrimination algorithm results using the two-waveband method for #4-finished SSS.

Dilution		#4-Finished SSS							
		Ratio Waveband [nm]		F-Value	Calibration			Validation	
					No. of Spectra	TH	Accuracy [%]	No. of Spectra	Accuracy [%]
Honeydew	original	612	676	3043	1702	0.55	90.64	425	90.61
	1:5	464	640	1349	1636	1.27	90.43	408	88.28
	1:10	464	640	1053	1531	1.11	90.53	382	87.74
	1:20	476	612	126	2052	0.74	82.77	512	81.93
	1:50	580	648	54	1460	0.50	62.19	365	62.46
	1:100	540	664	311	1465	0.33	59.61	366	59.60
Orange	original	472	612	387	1844	0.29	97.98	461	97.86
	1:5	476	664	1942	1771	2.06	91.03	442	91.94
	1:10	480	612	1326	1592	1.64	90.63	397	89.28
	1:20	464	600	1112	1987	1.13	89.03	496	89.94
	1:50	608	676	700	1527	0.22	88.35	381	88.14
	1:100	560	664	1779	1775	0.50	85.60	443	87.73
Apple	original	564	676	638	1672	0.14	84.12	418	84.18
	1:5	456	564	256	1861	0.26	74.19	465	74.37
	1:10	472	548	104	1763	0.22	74.03	440	73.93
	1:20	500	612	70	2076	0.41	64.86	518	64.74
	1:50	504	612	81	1570	1.48	65.11	392	61.30
	1:100	488	656	280	1431	0.24	58.17	357	58.05
Watermelon	original	464	728	428	2246	0.59	96.53	561	96.66
	1:5	464	616	1452	1555	1.08	90.52	388	84.17
	1:10	488	580	135	1551	0.55	89.31	387	89.81
	1:20	488	580	53	1984	0.55	88.59	495	89.15
	1:50	580	676	158	1576	2.48	82.60	394	82.84
	1:100	548	660	492	1471	1.01	74.52	367	76.86

Note: TH = Threshold value.

3.2.1. Development of Single-Waveband Algorithm (SWA)

Residue Detection Algorithm for Honeydew

A single-waveband algorithm (SWA) was developed to detect honeydew residue on the surface of 2B-finished SSS (Table 1). Figure S1a shows F-value of the one-way ANOVA for classifying 2B finished SS surface and honeydew residues. The resultant optimal wavebands for the original juice, and the 1:5, 1:10, and 1:20 dilution samples were close to 480 nm, and the threshold values for detecting the residues using the selected wavebands were 1983, 827, 545, and 362, respectively (Figure S1). The calibration accuracies were 92.92%, 91.56%, 86.86%, and 86.33%, and the validation accuracies were 92.94%, 91.45%, 86.99%, and 83.99%, respectively. The optimal wavebands for the 1:50 and 1:100 dilution samples were 684.4 nm, and the threshold values were 1742 and 1563, respectively. The calibration accuracies were 75.78% and 69.08%, and the validation accuracies were 70.46% and 67.25%, respectively. The 480-nm and 684-nm wavebands are related to carotenoids and chlorophyll, respectively [35–37].

For the SWA developed to detect honeydew residue on the surface of #4-finished SSS, the optimal waveband for the original juice was 508 nm, the threshold value was 1857, the calibration accuracy was 92.55%, and the validation accuracy was 92.54% (Figure S2a). The optimal wavebands for the 1:5, 1:10, 1:20, and 1:50 dilution samples were close to 480 nm, and the threshold values were 688, 429, 459, and 388, respectively. The calibration accuracies were 92.25%, 90.91%, 90.05%, and 69.73%, and the validation accuracies were 92.19%, 91.91%, 89.88%, and 63.42%, respectively. The optimal waveband for the original juice was 660 nm, the threshold value was 483, the calibration accuracy was 68.70%, and the validation accuracy was 65.64%. The 480-nm and 684-nm wavebands were related to carotenoids and chlorophyll-*a*, respectively [35–37].

Residue Detection Algorithm for Orange

For the SWA developed to detect orange residue on the surface of 2B-finished SSS, the optimal wavebands for the original juice, and the 1:5, 1:10, 1:20, and 1:50 dilution samples were close to 470 nm, and the threshold values for detecting the residues using the selected wavebands were 1891, 1242, 800, 495, and 332, respectively (Figure S1b). The calibration accuracies were 92.30%, 90.88%, 87.52%, 85.40%, and 80.08%, and the validation accuracies were 92.55%, 91.04%, 87.68%, 85.67%, and 80.01%, respectively. The optimal waveband for the original juice was 644 nm, the threshold value was 1585, the calibration accuracy was 72.55%, and the validation accuracy was 72.67%. The 470-nm and 644-nm wavebands were related to carotenoids and chlorophyll-*b*, respectively [35–37].

According to the SWA developed to detect orange residue on the surface of #4-finished SSS, the optimal waveband for the original juice was 492 nm, the threshold value was 620, the calibration accuracy was 98.23%, and the validation accuracy was 98.10% (Figure S2b). The optimal waveband for the 1:5, 1:10, and 1:20 dilution samples was 464 nm, and the threshold values were 1422, 1003, and 454, respectively. The calibration accuracies were 91.15%, 91.47%, and 92.98%, and the validation accuracies were 98.10%, 91.37%, and 91.66%, respectively. The optimal wavebands for the 1:50 and 1:100 dilution samples were 660 nm, and the threshold values were 577 and 994, respectively. The calibration accuracies were 92.72% and 89.81%, and the validation accuracies were 92.85% and 89.75%, respectively. 492-nm and 660-nm were related to carotenoids and chlorophyll-*b*, respectively [36,37].

Residue Detection Algorithm for Apple

For the SWA developed for detecting apple residue on the surface of 2B-finished SSS, the optimal waveband for the original juice, and the 1:5 and 1:10 dilution samples was 488 nm, and the threshold values for detecting the residues using the selected wavebands were 481, 415, and 382, respectively (Figure S1c). The calibration accuracies were 93.38%, 86.16% and 85.16% and the validation accuracies were 93.37%, 85.29% and 83.86%, respectively. The optimal wavebands for the 1:20, 1:50, and 1:100 dilution samples were close to 648 nm, and the threshold values for detecting the residues using the selected wavebands were 1707, 1556, and 1825, respectively. The 488-nm and 648-nm wavebands were related to carotenoids and chlorophyll-*b*, respectively [36,37].

For the SWA developed for detecting apple residue on the surface of #4-finished SSS, the optimal waveband for the original juice was 584 nm, the threshold value was 677, the calibration accuracy was 85.81%, and the validation accuracy was 85.17% (Figure S2c). The optimal wavebands for the 1:5 and 1:10 dilution samples were close to 470 nm, and the threshold values were 422 and 344, respectively. The calibration accuracies were 82.48% and 83.55%, and the validation accuracies were 79.47% and 72.34%, respectively. The optimal wavebands for the 1:20, 1:50, and 1:100 dilution samples were close to 660 nm, and the threshold values were 338, 437, and 487, respectively. The calibration accuracies were 80.63%, 71.83%, and 70.02%, and the validation accuracies were 77.48%, 70.04%, and 69.06%, respectively. The 470-nm and 660-nm wavebands were related to carotenoids and chlorophyll-*b*, respectively [36,37].

Residue Detection Algorithm for Watermelon

For the SWA developed to detect watermelon residue on the surface of 2B-finished SSS, the optimal wavebands for the original juice, and the 1:5, 1:10, and 1:20 dilution samples were close to 470 nm, and the threshold values for detecting the residues using the selected wavebands were 861, 487, 382, and 260, respectively (Figure S1d). The calibration accuracies were 85.35%, 82.74%, 82.94%, and 82.55%, and the validation accuracies were 85.73%, 82.71%, 82.78%, and 78.10%, respectively. The optimal wavebands for the 1:50 and 1:100 dilution samples were 644 nm, and the threshold values were 1555 and 1642, respectively. The calibration accuracies were 75.48% and 67.53%, and the validation accuracies were 70.55% and 60.02%, respectively. The 470-nm and 644-nm wavebands were related to carotenoids and chlorophyll-*b*, respectively [35–37].

For the SWA developed for detecting watermelon residue on the surface of 2B-finished SSS, the optimal wavebands for the original juice, and the 1:5, 1:10, and 1:20 dilution samples were close to 460 nm, and the threshold values for detecting the residues using the selected wavebands were 791, 434, 340, and 290, respectively (Figure S2d). The calibration accuracies were 89.04%, 87.71%, 88.54%, and 83.36%, and the validation accuracies were 89.22%, 86.91%, 86.03%, and 77.82%, respectively. The optimal wavebands for the 1:50 and 1:100 dilution samples were close to 660 nm, and the threshold values were 409 and 486, respectively. The calibration accuracies were 77.91% and 71.74%, and the validation accuracies were 69.30% and 70.76%, respectively. The 460-nm and 660-nm wavebands were related to carotenoids and chlorophyll-*b*, respectively [35–37].

Tables 1 and 2 summarize the results of the ANOVA analysis performed to determine the optimal wavelengths to detect different samples. First, when the SWA was applied, the optimal wavebands for each of the dilution samples were similarly selected on the surfaces of 2B-finished SSS and #4-finished SSS. For honeydew, orange, and watermelon, the optimal wavebands for the original juice and the 1:5, 1:10, and 1:20 dilution samples were in the 470–500 nm range, and the optimal wavebands for the 1:50 and 1:100 dilution samples were in the 660–680 nm range. For apple, the optimal wavebands for original juice, and the 1:5 and 1:10 dilution samples were in the 480–490 nm range, and the optimal wavebands for the 1:20, 1:50, and 1:100 dilution samples were in the 648–660 nm range. The lower the dilution levels on both surfaces, the lower was the accuracy of the selected waveband.

In order to determine whether the accuracy was higher when using a single waveband or multiple wavebands, the optimal wavebands were selected using the ratio algorithm (Tables 3 and 4).

3.2.2. Development of the Two-Waveband Ratio Algorithm (TWRA)

Residue Detection Algorithm for Honeydew

A two-waveband ratio algorithm (TWRA) was developed to detect honeydew residue on the surface of 2B-finished SSS. The resultant optimal wavebands for the original juice up to the 1:100 dilution samples were in the 460–480 nm and 650–680 nm ranges (Figure S3). The TWRA calibration accuracies were 91.79%, 90.56%, 87.51%, 85.40%, 75.19%, and 74.84% with threshold values of 0.98, 0.40, 0.34, 0.18, 0.15, and 0.14, and validation accuracies of 92.44%, 91.63%, 88.67%, 84.36%, 78.23%, and 73.43%, respectively, for the original juice and the 1:5, 1:10, 1:20, 1:50, and 1:100 dilutions.

For the TWRA developed to detect honeydew residue on the surface of #4-finished SSS, the optimal wavebands for the original juice were 612 nm and 676 nm (Figure S7). The TWRA calibration accuracy was 90.64% with a threshold value of 0.55 and validation accuracy of 90.61%. The optimal wavebands for the 1:5, 1:10, and 1:20 dilution samples were in the 460–480 nm and 610–640 nm ranges. The TWRA calibration accuracies were 90.43%, 90.53%, and 82.77% with threshold values of 1.27, 1.11, and 0.74, and validation accuracies of 88.28%, 87.74%, and 81.93%, respectively, for these samples. The optimal wavebands for the 1:50 and 1:100 dilution samples were in the 540–580 nm and 640–670 nm ranges. The TWRA calibration accuracies were 62.19% and 59.61% with threshold values of 0.50 and 0.33, and validation accuracies of 62.46% and 59.60%, respectively.

Residue Detection Algorithm for Orange

For the TWRA developed to detect orange residue on the surface of 2B-finished SSS, the optimal waveband for the original juice and dilution samples up to 1:100 were in the 460–480 nm and 640–660 nm ranges (Figure S4). The TWRA calibration accuracies were 92.30%, 90.96% 90.06%, 88.48%, 84.90%, and 74.37% with threshold values of 0.43, 0.63, 0.44, 0.28, 0.17, and 0.17, and validation accuracies of 92.36%, 91.84%, 90.36%, 88.62%, 85.79%, and 72.02%, respectively, for the original juice and the 1:5, 1:10, 1:20, 1:50, and 1:100 dilutions.

Based on the TWRA developed to detect orange residue on the surface of #4 finished SSS, the optimal wavebands for original juice, and the 1:5, 1:10 and 1:20 dilution samples were in the 450–470 nm and 610–660 nm ranges (Figure S8). The TWRA calibration accuracies were 97.98%, 91.03%, 90.63%, and 89.03% with threshold values of 0.29, 2.06, 1.64, and 1.13, and validation accuracies of 97.86%, 91.94%, 89.28%, and 89.94%, for these samples. The optimal wavebands for the 1:50 and 1:100 dilution samples were in the 560–608 nm and 664–676 nm ranges. The TWRA calibration accuracies were 88.35% and 88.14% with threshold values of 0.22 and 0.50, and validation accuracies of 88.14% and 87.73%, respectively.

Residue Detection Algorithm for Apple

For the TWRA developed for detecting apple residue on the surface of 2B-finished SSS, the optimal wavebands for the original juice and dilution samples up to 1:100 were in the 460–490 nm and 640–660 nm ranges (Figure S5). The TWRA calibration accuracies were 93.12%, 89.07%, 88.22%, 87.63%, 83.95%, and 77.02% with threshold values of 0.21, 0.70, 0.20, 0.16, 0.19, and 0.11, and validation accuracies of 92.90%, 89.53%, 87.53%, 83.90%, 76.09% and 72.91%, respectively, for the original juice and the 1:5, 1:10, 1:20, 1:50, and 1:100 dilutions.

For the TWRA developed for detecting apple residue on the surface of #4-finished SSS, the optimal wavebands for the original juice were 564 nm and 676 nm (Figure S9). The TWRA calibration accuracy was 84.12% with a threshold value of 0.14 and validation accuracy of 84.18%. The optimal wavebands for the 1:5 and 1:10 dilution samples were in the 456–472 nm and 548–564 nm ranges. The TWRA calibration accuracies were 74.19% and 74.03% with threshold values of 0.26 and 0.22, and validation accuracies of 74.37% and 73.93%, respectively. The optimal wavebands for the 1:20, 1:50, and 1:100 dilution samples were 488–505 nm and 612–656 nm. The TWRA calibration accuracies were 64.86%, 65.11%, and 58.17% with threshold values of 0.41, 1.48 and 0.2, and validation accuracies of 64.74%, 61.30%, and 58.05%, respectively.

Residue Detection Algorithm for Watermelon

For the TWRA developed for detecting watermelon residue on the surface of 2B-finished SSS, the optimal wavebands for the original juice and dilution samples up to 1:100 were in the 460–480 nm and 630–660 nm ranges (Figure S6). The TWRA calibration accuracies were 87.31%, 87.15%, 87.31%, 84.39%, 77.57%, and 64.71% with threshold values of 0.56, 0.41, 0.32, 0.20, 0.18, and 0.70, and validation accuracies of 93.31%, 90.67%, 87.45%, 82.06%, 80.33%, and 63.36%, respectively, for the original juice and the 1:5, 1:10, 1:20, 1:50, and 1:100 dilutions.

For the TWRA developed for detecting watermelon residue on the surface of #4-finished SSS, the optimal wavebands for the original juice and dilution samples up to 1:20 were 460–490 nm, 728 nm, and 580–616 nm (Figure S10). The TWRA calibration accuracies were 96.53%, 90.52%, 89.31%, and 88.59% with threshold values of 0.59, 1.08, 0.55, and 0.55, and validation accuracies of 96.66%, 84.17%, 89.81%, and 89.15%, respectively. The optimal wavebands for the 1:50 and 1:100 dilution samples were in the 548–580 nm and 660–676 nm ranges. The TWRA calibration accuracies were 82.60% and 74.52% with threshold values of 2.48 and 1.0, and validation accuracies of 82.84% and 76.86%, respectively.

Similar to the SWA results, the lower was the dilution concentration on both surfaces, the lower was the accuracy of the selected waveband. In the TWRA, consistent wavebands were selected for the 2B -finished SS surface. The detection accuracy for the original juices was high; however, the accuracy tended to decrease with juice concentration.

3.2.3. Development of Global Imaging Algorithm for Detecting Residues

Based on these results, an algorithm was developed that allows the selected wavelengths to be applied for concentration, regardless of the type of fruit. The SWA was initially applied (Table 5). On the 2B-finished SS surface, a detection accuracy of 93.37%

was obtained when a threshold value of 482 was applied at 488 nm for the original juices. Detection accuracies of 92.42%, 90.91%, and 83.34% were obtained when threshold values of 670, 545, and 382 were applied, respectively, at 484 nm for the 1:5 up to 1:20 dilution samples, respectively. For the 1:50 and 1:100 dilution samples, detection accuracies of 62.51% and 55.81% were obtained when thresholds values of 1633 and 1685 at 644 nm, were applied, respectively. On the #4-finished SS surface, the original juices were detected at an accuracy of 84.43%, when a threshold value of 670 was applied at 460 nm. Detection accuracies of 90.74%, 83.31%, and 75.71% were obtained when the threshold values of 611, 594, and 549 were applied at 484 nm for the 1:5 up to 1:20 dilution samples, respectively. For the 1:50 dilution sample at 652 nm and the 1:100 dilution sample at 660 nm, detection accuracies of 68.41% and 80.95% were obtained when threshold values of 301 and 332 were applied, respectively. For the detection of fruit residue, the 460 nm and 484 nm wavelengths related to carotenoids were selected for a 1:20 dilution concentration of the original juice, and 644–660 nm related to chlorophyll was selected for a dilution concentration of 1:50–1:100 [35–37].

Table 5. Optimal single waveband and discrimination algorithm results for all the samples according to the dilution levels.

Total	2B-Finished SSS				#4-Finished SSS			
	No of Sample	Single Waveband [nm]	TH	Accuracy [%]	No of Sample	Single Waveband [nm]	TH	Accuracy [%]
original	7533	488	482	93.37	9329	460	670	84.43
1:5	8140	484	670	92.42	8526	464	611	90.74
1:10	7825	484	545	90.91	8043	464	594	83.31
1:20	7719	484	382	83.34	10,120	464	549	75.71
1:50	7141	644	1633	62.51	7665	652	301	68.41
1:100	6935	644	1685	55.81	7675	660	332	80.95

Note: TH = Threshold value.

Table 6 shows the results of applying the integrated wavebands using the TWRA. On the 2B-finished SS surface, detection accuracies of 92.49%, 88.07%, 86.53%, 86.92%, 76.52%, and 61.14% were obtained for original juices up to 1:100 dilution samples when the threshold values of 0.36, 0.32, 0.30, 0.28, 0.28, and 0.27 were applied in the combination of 460 nm and 656 nm, 460 nm and 652 nm, 472nm and 644 nm, 468 nm and 648 nm, 468 nm and 652 nm, 472 nm and 652 nm, respectively. On the #4-finished SS surface, detection accuracies of 75.80%, 52.97%, 65.63%, 57.57%, 60.05%, and 58.09% were obtained for original juices up to 1:100 dilution samples when the threshold values of 1.31, 0.42, 1.69, 0.72, 0.45, and 0.24 were applied in the combinations of 488 nm and 676 nm, 464 nm and 612 nm, 476 nm and 580 nm, 476 nm and 612 nm, 580 nm and 676 nm, 560 nm and 664 nm, respectively. The combination of 460 nm and 650 nm was selected for the 2B-finished SS surface. The difference between the wavebands selected at each dilution concentration and the wavebands selected at the total dilution concentration on the 2B-finished SS surface was not greater than that on the #4-finished SS surface. Therefore, the integrated algorithms for the 2B-finished SS surface exhibited better detection accuracies than those for the #4-finished SS surface.

Table 6. Optimal two wavebands and discrimination algorithm results for all the samples according to the dilution levels.

Total	2B-Finished SSS					#4-Finished SSS				
	No of Sample	Ratio Waveband [nm]		TH	Accuracy [%]	No of Sample	Ratio Waveband [nm]		TH	Accuracy [%]
original	7533	460.8	656.4	0.36	92.49	9329	488.8	676.4	1.31	75.80
1:5	8140	460.8	652.4	0.32	88.07	8526	464.8	612.5	0.42	54.97
1:10	7825	472.8	644.5	0.30	86.53	8043	476.8	580.6	1.69	65.63
1:20	7719	468.8	648.4	0.28	86.92	10,120	476.8	612.5	0.72	57.57
1:50	7141	468.8	652.4	0.28	76.52	7665	580.6	676.4	0.45	60.05
1:100	6935	472.8	652.4	0.27	61.14	7675	560.6	664.4	0.24	58.09

Note: TH = Threshold value.

Figure 6 shows an example of the process in which an image is applied at the selected wavelength using ANOVA analysis. The threshold value determined using the TWRA is applied after acquiring the ratio image with the selected single-wavelength images. The obtained binary image renders it possible to determine whether the residues are detected by expressing the part recognized as detected in white and the part recognized as missing in black.

An imaging algorithm to detect fruit residue contamination was developed using the waveband image selected through ANOVA analysis. Figure 6 illustrates the image processing that was performed to detect residues using a two-band ratio image. If a residue is present, the binary image is '1', otherwise it is '0'. Figure 7 shows the determination of residue contamination based on the concentration for four types of fruit. These results establish the possibility of using fluorescence imaging techniques to detect organic residues that may be present in food processing equipment, even after cleaning and sterilization.

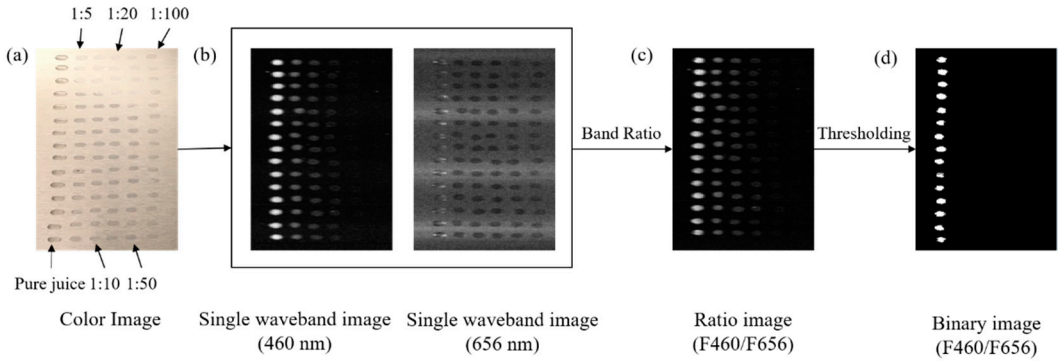

Figure 6. Image processing for classification of fruit residues on stainless steel: (**a**) The hyperspectral fluorescence images are acquired, (**b**) the single-band images are selected, (**c**) the two-waveband images are obtained, and (**d**) the binary images are acquired by applying a threshold value and the residue is detected.

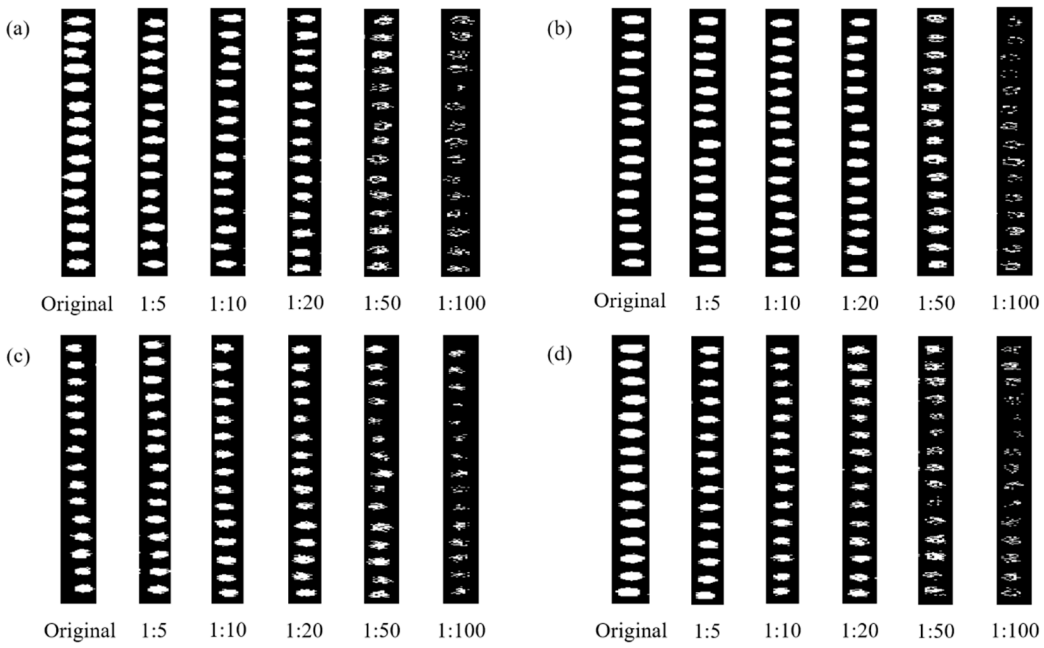

Figure 7. Discrimination image applied global imaging algorithms for juice dilution levels of each fruit (**a**) honeydew, (**b**) orange, (**c**) apple and (**d**) watermelon.

Table 7 shows the results of image discrimination applied with the integrated TWRA. The discrimination accuracy of the integrated image model for the 2B-finished SSS was 100%, 99.17%, and 95% for original juices up to 1:20 dilution samples, 1:50 dilution samples, and 1:100 dilution samples, respectively. The discrimination accuracy of the integrated image model for the #4-finished SSS was 100%, 94.17%, 93.89%, and 89.44% for original juices up to 1:10 dilution samples, 1:20 dilution samples, 1:50 dilution samples, and 1:100 dilution samples, respectively. The image-based discrimination result showed better performance than the spectrum-based discrimination result. Also, residue detection performance was better for the 2B-finished SS surface than for the #4-finished SS surface.

Table 7. Discrimination accuracy from image using global two-band ratio algorithm.

	Dilution	2B-Finished SSS			#4-Finished SSS		
		No. of Droplet	No. of Detection	Accuracy [%]	No. of Droplet	No. of Detection	Accuracy [%]
Honeydew	original	90	90	100.0	90	90	100.0
	1:5	90	90	100.0	90	90	100.0
	1:10	90	90	100.0	90	90	100.0
	1:20	90	90	100.0	90	87	96.67
	1:50	90	90	100.0	90	86	95.56
	1:100	90	86	95.56	90	83	92.22
Orange	original	90	90	100.0	90	90	100.0
	1:5	90	90	100.0	90	90	100.0
	1:10	90	90	100.0	90	90	100.0
	1:20	90	90	100.0	90	90	100.0
	1:50	90	90	100.0	90	90	100.0
	1:100	90	90	100.0	90	90	100.0
Apple	original	90	90	100.0	90	90	100.0
	1:5	90	90	100.0	90	90	100.0
	1:10	90	90	100.0	90	90	100.0
	1:20	90	90	100.0	90	78	86.67
	1:50	90	90	100.0	90	78	86.67
	1:100	90	85	94.44	90	74	82.22
Watermelon	original	90	90	100.0	90	90	100.0
	1:5	90	90	100.0	90	90	100.0
	1:10	90	90	100.0	90	90	100.0
	1:20	90	90	100.0	90	84	93.33
	1:50	90	87	96.67	90	84	93.33
	1:100	90	81	90.00	90	75	83.33
Total sample	original	360	360	100.0	360	360	100.0
	1:5	360	360	100.0	360	360	100.0
	1:10	360	360	100.0	360	360	100.0
	1:20	360	360	100.0	360	339	94.17
	1:50	360	357	99.17	360	338	93.89
	1:100	360	342	95.00	360	322	89.44

4. Conclusions

In this study, a hyperspectral fluorescence imaging technique was developed for the rapid detection of food residues that can remain as contaminants on the surfaces of food processing equipment. A technique was developed for rapidly detecting apple, orange, melon, and watermelon residue that may remain on the surfaces of 2B- and #4-finished stainless steel sheets, which are commonly used for food processing equipment. These two types of stainless-steel surfaces have different fluorescence spectral characteristics. Analyses for the optimal wavelength using ANOVA indicated that the accuracy for 2B-finished SSS was greater than that of #4-finished SSS. Compared to the SWA, the detection accuracy of the TWRA was slightly higher or similar. The discrimination accuracy of the integrated image model to detect the organic residue of all fruits on the 2B-finished SSS was 100% and above 95%, respectively, for original juices up to 1:20 dilution samples and for 1:50–1:100 dilution samples, respectively. By combining these results, global wavebands were selected according to the dilution levels, regardless of the type of fruit. Moreover,

the detection accuracy on the 2B-finished surface was higher than that on the #4-finished surface. Based on these results, an algorithm will be developed that can be applied to organic residue of various fresh-cut fruits and vegetables in the future.

The results of this study establish the possibility of using fluorescence imaging techniques to detect residues that may be present in food processing equipment, even after cleaning and sterilization [6]. Fluorescence imaging can be applied for testing the presence of organic residues of various agricultural products by detecting microgram quantities. In addition, the results show that sanitation monitoring for residues is possible. Therefore, the results of this study can be applied to the development of a multispectral imaging system to detect the residue of fresh-cut foods in food processing plants.

Supplementary Materials: The following are available online at https://www.mdpi.com/2076-3417/11/1/458/s1, Figure S1: Results of one-way ANOVA for classifying 2B finished stainless steel surface and residues of (a) honeydew, (b) orange, (c) apple, and (d) watermelon using the single waveband algorithm. Figure S2: Results of one-way ANOVA for classifying #4 finished stainless steel surface and residues of (a) honeydew, (b) orange, (c) apple, and (d) watermelon using the single waveband algorithm. Figure S3: Results of one-way ANOVA for classifying 2B finished stainless steel surface and honeydew residue dilutions((a) 1:1, (b) 1:5, (c) 1:10, (d) 1:20, (e) 1:50, and (f) 1:100) using the two wavebands ratio algorithm. Figure S4: Results of one-way ANOVA for classifying 2B finished stainless steel surface and orange residue dilutions((a) 1:1, (b) 1:5, (c) 1:10, (d) 1:20, (e) 1:50, and (f) 1:100) using the two wavebands ratio algorithm. Figure S5: Results of one-way ANOVA for classifying 2B finished stainless steel surface and apple residue dilutions((a) 1:1, (b) 1:5, (c) 1:10, (d) 1:20, (e) 1:50, and (f) 1:100) using the two wavebands ratio algorithm. Figure S6: Results of one-way ANOVA for classifying 2B finished stainless steel surface and watermelon residue dilutions((a) 1:1, (b) 1:5, (c) 1:10, (d) 1:20, (e) 1:50, and (f) 1:100) using the two wavebands ratio algorithm. Figure S7: Results of one-way ANOVA for classifying #4 finished stainless steel surface and honeydew residue dilutions((a) 1:1, (b) 1:5, (c) 1:10, (d) 1:20, (e) 1:50, and (f) 1:100) using the two wavebands ratio algorithm. Figure S8: Results of one-way ANOVA for classifying #4 finished stainless steel surface and orange residue dilutions((a) 1:1, (b) 1:5, (c) 1:10, (d) 1:20, (e) 1:50, and (f) 1:100) using the two wavebands ratio algorithm. Figure S9: Results of one-way ANOVA for classifying #4 finished stainless steel surface and apple residue dilutions((a) 1:1, (b) 1:5, (c) 1:10, (d) 1:20, (e) 1:50, and (f) 1:100) using the two wavebands ratio algorithm. Figure S10: Results of one-way ANOVA for classifying #4 finished stainless steel surface and watermelon residue dilutions((a) 1:1, (b) 1:5, (c) 1:10, (d) 1:20, (e) 1:50, and (f) 1:100) using the two wavebands ratio algorithm.

Author Contributions: Experiment design and execution, manuscript writing/review, C.H., C.M., J.L.; analysis, Y.S., I.B.; project administration, M.S.K.; All authors have read and agreed to the published version of the manuscript.

Funding: This research was supported by the research program for Agricultural Science and Technology Development (Grant No. PJ012216), National Institute of Agricultural Sciences, Rural Development Administration, Republic of Korea.

Data Availability Statement: The data presented in this study are available within the article and its Supplementary Materials.

Acknowledgments: The authors would like to thank Diane Chan of the Environmental Microbial and Food Safety Laboratory, ARS, USDA, for proofreading the manuscript.

Conflicts of Interest: The authors declare no conflict of interest.

References

1. Lee, H.-H.; Hong, S.-I.; Kim, D. Microbiological and visual quality of fresh-cut cabbage as affected by packaging treatments. *Food Sci. Biotechnol.* **2011**, *20*, 229–235. [CrossRef]
2. Vargas, A.M.; Kim, M.S.; Tao, Y.; Lefcourt, A.M.; Chen, Y.R.; Luo, Y.; Song, Y.; Buchanan, R. Detection of fecal contamination on cantaloupes using hyperspectral fluorescence imagery. *J. Food Sci.* **2005**, *70*, e471–e476. [CrossRef]
3. Mo, C.; Kim, G.; Kim, M.S.; Lim, J.; Lee, S.H.; Lee, H.-S.; Cho, B.-K. Discrimination methods for biological contaminants in fresh-cut lettuce based on VNIR and NIR hyperspectral imaging. *Infrared Phys. Technol.* **2017**, *85*, 1–12. [CrossRef]

4. Lopez-Velasco, G.; Sbodio, A.; Tomás-Callejas, A.; Wei, P.; Tan, K.H.; Suslow, T.V. Assessment of root uptake and systemic vine-transport of Salmonella enterica sv. Typhimurium by melon (Cucumis melo) during field production. *Int. J. Food Microbiol.* **2012**, *158*, 65–72. [CrossRef]
5. Qadri, O.S.; Yousuf, B.; Srivastava, A.K.; Yildiz, F. Fresh-cut fruits and vegetables: Critical factors influencing microbiology and novel approaches to prevent microbial risks—A review. *Cogent Food Agric.* **2015**, *1*, 1–11. [CrossRef]
6. Wiederoder, M.S.; Lefcourt, A.M.; Kim, M.S.; Lo, Y.M. Detection of fresh-cut produce processing residues on food contact surface materials using hyperspectral imaging. *J. Food Meas. Charact.* **2012**, *6*, 48–55. [CrossRef]
7. Kuda, T.; Shibata, G.; Takahashi, H.; Kimura, B. Effect of quantity of food residues on resistance to desiccation of food-related pathogens adhered to a stainless steel surface. *Food Microbiol.* **2015**, *46*, 234–238. [CrossRef]
8. Kuda, T.; Koyanagi, T.; Shibata, G.; Takahashi, H.; Kimura, B. Effect of carrot residue on the desiccation and disinfectant resistances of food related pathogens adhered to a stainless steel surfaces. *LWT Food Sci.* **2016**, *74*, 251–254. [CrossRef]
9. Wiederoder, M.S. Portable Hyperspectral Imaging Device for Surface Sanitation Verification in the Produce Industry. Master's Thesis, University of Maryland, Collage Park, MD, USA, 2011.
10. Bonah, E.; Huang, X.; Aheto, J.H.; Osae, R. Application of hyperspectral imaging as a nondestructive technique for foodborne pathogen detection and characterization. *Foodborne Pathog. Dis.* **2019**, *16*, 712–722. [CrossRef]
11. Zhao, X.; Lin, C.-W.; Wang, J.; Oh, D.H. Advances in rapid detection methods for doodborne pathogens. *J. Microbiol. Biotechnol.* **2014**, *24*, 297–312. [CrossRef]
12. Zhao, X.; Li, M.; Xu, Z. Detection of foodborne pathogens by surface enhanced raman spectroscopy. *Front. Microbiol.* **2018**, *9*, 1236. [CrossRef] [PubMed]
13. Law, J.W.-F.; Ab Mutalib, N.-S.; Chan, K.-G.; Lee, L.-H. Rapid methods for the detection of foodborne bacterial pathogens: Principles, applications, advantages and limitations. *Front. Microbiol.* **2014**, *5*, 770. [CrossRef] [PubMed]
14. Wiederoder, M.S.; Liu, N.; Lefcourt, A.M.; Kim, M.S.; Martin Lo, Y. Use of a portable hyperspectral imaging system for monitoring the efficacy of sanitation procedures in produce processing plants. *J. Food Eng.* **2013**, *117*, 217–226. [CrossRef]
15. Jun, W.; Kim, M.S.; Lee, K.; Millner, P.; Chao, K. Assessment of bacterial biofilm on stainless steel by hyperspectral fluorescence imaging. *Sens. Instrum. Food Qual. Saf.* **2009**, *3*, 41–48. [CrossRef]
16. Kim, M.S.; Chen, Y.R.; Mehl, P.M. Hyperspectral reflectance and fluorescence imaging system for food quality and safety. *Trans. ASAE* **2001**, *44*, 721. [CrossRef]
17. Qin, J.; Chao, K.; Kim, M.S.; Lu, R.; Burks, T.F. Hyperspectral and multispectral imaging for evaluating food safety and quality. *J. Food Eng.* **2013**, *118*, 157–171. [CrossRef]
18. Lee, W.-H.; Kim, M.S.; Lee, H.; Delwiche, S.R.; Bae, H.; Kim, D.-Y.; Cho, B.-K. Hyperspectral near-infrared imaging for the detection of physical damages of pear. *J. Food Eng.* **2014**, *130*, 1–7. [CrossRef]
19. Kamruzzaman, M.; Elmasry, G.; Sun, D.-W.; Allen, P. Non-destructive prediction and visualization of chemical composition in lamb meat using NIR hyperspectral imaging and multivariate regression. *Innov. Food Sci. Emerg. Technol.* **2012**, *16*, 218–226. [CrossRef]
20. Elmasry, G.; Kamruzzaman, M.; Sun, D.-W.; Allen, P. Principles and applications of hyperspectral imaging in quality evaluation of agro-food products: A review. *Crit. Rev. Food Sci. Nutr.* **2012**, *52*, 999–1023. [CrossRef]
21. Xing, J.; Bravo, C.; Jancsók, P.T.; Ramon, H.; De Baerdemaeker, J. Detecting bruises on 'golden delicious' apples using hyperspectral imaging with multiple wavebands. *Biosyst. Eng.* **2005**, *90*, 27–36. [CrossRef]
22. Cho, B.-K.; Kim, M.S.; Baek, I.-S.; Kim, D.-Y.; Lee, W.-H.; Kim, J.; Bae, H.; Kim, Y.-S. Detection of cuticle defects on cherry tomatoes using hyperspectral fluorescence imagery. *Postharvest Biol. Technol.* **2013**, *76*, 40–49. [CrossRef]
23. Qin, J.; Kim, M.S.; Chao, K.; Chan, D.E.; Delwiche, S.R.; Cho, B.-K. Line-scan hyperspectral imaging techniques for food safety and quality applications. *Appl. Sci.* **2017**, *7*, 125. [CrossRef]
24. Qin, J.; Burks, T.F.; Kim, M.S.; Chao, K.; Ritenour, M.A. Citrus canker detection using hyperspectral reflectance imaging and PCA-based image classification method. *Sens. Instrum. Food Qual. Saf.* **2008**, *2*, 168–177. [CrossRef]
25. Lee, M.S.; Kim, K.S.; Min, G.; Son, D.H.; Kim, J.E.; Kim, S.C. Recent trends of hyperspectral imaging technology. *ETRI* **2019**, *34*, 86–97. [CrossRef]
26. Cho, H.; Lee, H.; Kim, S.-Y.; Kim, D.; Lefcourt, A.M.; Chan, D.E.; Chung, S.; Kim, M.S. Potential application of fluorescence imaging for assessing fecal contamination of soil and compost maturity. *Appl. Sci.* **2016**, *6*, 243. [CrossRef]
27. Qin, J.; Chao, K.; Kim, M.S.; Kang, S.; Cho, B.-K.; Jun, W. Detection of organic residues on poultry processing equipment surfaces by LED-induced fluorescence imaging. *Appl. Eng. Agric.* **2011**, *27*, 153–161. [CrossRef]
28. Zhang, R.; Ying, Y.; Rao, X.; Li, J. Quality and safety assessment of food and agricultural products by hyperspectral fluorescence imaging. *J. Sci. Food Agric.* **2012**, *92*, 2397–2408. [CrossRef]
29. Everard, C.D.; Kim, M.S.; Lee, H. A comparison of hyperspectral reflectance and fluorescence imaging techniques for detection of contaminants on spinach leaves. *J. Food Eng.* **2014**, *143*, 139–145. [CrossRef]
30. Mo, C.; Kim, G.; Kim, M.S.; Lim, J.; Lee, K.; Lee, W.-H.; Cho, B.-K. On-line fresh-cut lettuce quality measurement system using hyperspectral imaging. *Biosyst. Eng.* **2017**, *156*, 38–50. [CrossRef]
31. Cho, B.; Kim, M.S.; Chao, K.; Lawrence, K.; Park, B.; Kim, K. Detection of fecal residue on poultry carcasses by laser-induced fluorescence imaging. *J. Food Sci.* **2009**, *74*, E154–E159. [CrossRef]

32. Frank, J.F.; Chmielewski, R. Influence of surface finish on the cleanability of stainless steel. *J. Food Prot.* **2001**, *64*, 1178–1182. [CrossRef] [PubMed]
33. Mo, C.; Kim, M.S.; Kim, G.; Cheong, E.J.; Yang, J.; Lim, J. Detecting drought stress in soybean plants using hyperspectral fluorescence imaging. *J. Biosyst. Eng.* **2015**, *40*, 335–344. [CrossRef]
34. Ryerson: Metal Processing & Distribution. Finish, Finish, Finish: 3 Stainless Steel Finishes. Available online: https://www.ryerson.com/resource/the-gauge/three-layers-of-stainless-steel-polish (accessed on 24 December 2020).
35. Tadmor, Y.; Burger, J.; Yaakov, I.; Feder, A.; Libhaber, S.E.; Portnoy, V.; Meir, A.; Tzuri, G.; Sa'Ar, U.; Rogachev, I.; et al. Genetics of flavonoid, carotenoid, and chlorophyll pigments in melon fruit rinds. *J. Agric. Food Chem.* **2010**, *58*, 10722–10728. [CrossRef] [PubMed]
36. Gross, J. *Pigments in Vegetables: Chlorohylls and Carotenoids*; Van Nostrand Reinhold: New York, NY, USA, 1991.
37. Merzlyak, M.N.; Melø, T.B.; Naqvi, K.R. Effect of anthocyanins, carotenoids, and flavonols on chlorophyll fluorescence excitation spectra in apple fruit: Signature analysis, assessment, modelling, and relevance to photoprotection. *J. Exp. Bot.* **2008**, *59*, 349–359. [CrossRef] [PubMed]
38. Lamb, J.J.; Rokke, G.; Hohmann-Marriott, M.F. Chlorophyll fluorescence emission spectroscopy of oxygenic organisms at 77 K. *Photosynthetica* **2018**, *56*, 105–124. [CrossRef]
39. Wang, B.; Shen, J.; Huang, Y.; Liu, Z.; Zhuang, H. Graphene quantum dots and enzyme-coupled biosensor for highly sensitive determination of hydrogen peroxide and glucose. *Int. J. Mol. Sci.* **2018**, *19*, 1696. [CrossRef]
40. Muharfiza; Al Riza, D.F.; Saito, Y.; Itakura, K.; Kohno, Y.; Suzuki, T.; Kuramoto, M.; Kondo, N. Monitoring of fluorescence characteristics of satsuma mandarin (Citrus unshiu Marc.) during the maturation period. *Horticulturae* **2017**, *3*, 51. [CrossRef]
41. Yoo, K.S.; Bang, H.; Lee, E.J.; Crosby, K.M.; Patil, B.S. Variation of carotenoid, sugar, and ascorbic acid concentrations in watermelon genotypes and genetic analysis. *Hortic. Environ. Biotechnol.* **2012**, *53*, 552–560. [CrossRef]
42. Mukai, R.; Terao, J.; Shirai, Y.; Saito, N.; Ashida, H. Determination of subcellular localization of flavonol in cultured cells by laser scanning. In *Laser Scanning, Theory and Applications*; Wang, C.-C., Ed.; IntechOpen, Ltd.: London, UK, 2011. [CrossRef]
43. Włodarska, K.; Pawlak-Lemańska, K.; Khmelinskii, I.; Sikorska, E. Explorative study of apple juice fluorescence in relation to antioxidant properties. *Food Chem.* **2016**, *210*, 593–599. [CrossRef]